PNAS RESEARCH ARTICLE | ENGINEERING

A self-wrapping, bioresorbable neural interface for wireless multimodal therapy of localized peripheral nerve injury

Pengchuan Liu[a,b,c,1], Lianjie Zhou[a,b,c,1], Dian Xu[d,1], Dongqi An[d], Yifei Lu[a,b,c], Bofan Hu[a,b,c], Yuting Shao[e], Ningge Huang[a,b,c], Chengjie Guo[d], Li Chen[b,c], Jinbao Li[d], Jiahao Li[a,b,c], Fuying Liang[a,b], Junhan Liu[a,b,c], Gaoshan Huang[a,b,c], Yongfeng Mei[a,b,c], Rui Li[d,2], and Enming Song[a,b,c,f,g,2]

Affiliations are included on p. 10.

Edited by John Rogers, Northwestern University–Evanston, Evanston, IL; received August 10, 2025; accepted December 8, 2025

High-precision in vivo therapeutic technologies that establish three-dimensional (3D), multimodal neural interfaces with targeted biotissues offer significant clinical potential for the timely treatments of localized peripheral nerve injury (PNI). Current approaches for this purpose such as implantable devices face challenges in terms of percutaneous wires and/or nondegradable designs, and support only single-mode operation that lack microscale spatial resolution. Here, we develop a miniaturized, self-wrapping system that yields wireless, multimodal neural interfaces with 3D adaptation across localized peripheral nerves at scales ranging from tens of micrometers (15 μm) to millimeters. Such platform integrates multilayer architectures that include SiN_x layers as the mechanically triggered substrate for 3D wrapping, with multimodal treatments via MXene and drug-loaded layers for photothermal stimulation and pharmacological release. Experimental and computational studies establish operational principle as the basis for the combination of long-term photothermal therapy and transient drug delivery at high spatiotemporal resolution. In vivo tests on living rat models demonstrate that the implantable neural interface can roll up across the localized, dynamic surface of injured nerves, providing sustained treatments over 1 mo in a fully bioresorbable design after the healing process. These findings create future opportunities of such wireless, multimodal system with 3D self-wrapping techniques for precise PNI therapeutic strategies.

self-wrapping bistable neural interface | peripheral nerve repair | photothermal therapy | drug delivery | bioresorbable electronics

Significance

Emerging classes of high-precision, bioresorbable systems for in vivo treatment of localized peripheral nerve injury mark a significant advance in neural engineering. Critical challenges remain in development of three-dimensional, wireless platforms that establish adaptive interfaces to targeted injured nerves for high-resolution therapy. This work introduces a self-wrapping, multimodal neural interface that combines near-infrared photothermal stimulation with sustained drug delivery in microscale, rolled-up platforms. Such implants can be mechanically triggered to conform to localized nerve regions at diameters from 15 μm to 1 mm, adapting seamlessly in fully bioresorbable designs. In vivo studies in rat models demonstrate dynamic, multimodal modulation of nerve repair over extended timescales. This work establishes framework of minimally-invasive neurotherapeutics for nerve injury under various conditions.

Advanced technologies for high-precision, in vivo treatments of localized peripheral nerve injury (PNI) provide broad utility both in biomedical research as well as in clinical practice (1, 2). An important focus is on the establishment of high-performance neural interfaces that enable timely, multimodal therapy as the basis for healing processes of the injured tissue (3, 4). For example, microsurgical procedures (such as nerve suturing or autologous nerve grafting) stand for the clinical gold-standard for PNI repair; however, they demand a high level of microsurgical expertise, extensive preoperative preparation, and costly equipment (5). Additionally, the insertion of sutures into nerve tissue can impede axonal regrowth, and the technical difficulty increases dramatically when dealing with fine nerves tens to hundreds of micrometers in diameter (6). Alternative methods such as electrical stimulation offer attractive strategies for accelerating tissue-functional recovery, for inducing neurotrophic factor secretion, and for chronic PNI management (7). Although useful, conventional means for electrical stimulation typically rely on rigid, wired electrodes, and external power supplies, transmitting pulsed signals through wires and bulky designs, which restricts natural movement and thus limits clinical feasibility (8).

Emerging classes of biointegrated optical/electrical neural interfaces provide powerful capabilities (9–11), owing to their ability ranging from adaptive formation of three-dimensional (3D) coverage across neural fibers (12), to high-level integration of multiple operational modalities, and to full biodegradation of constituent materials after in vivo therapy (13–15). Recent research establishes a variety of in vivo shape-morphing, self-wrapping implantable systems in this context. Embodiments range from shape-memory-polymer sheets with temperature-triggered wrapping across sciatic nerve for neuromodulation (16), to silicon-membrane-based electrodes as restorative peripheral neural interface (17), and to electrochemically actuated 3D conductive polymers for treatments of neuropathic injuries (18). These platforms typically focus on large millimeter-scale operation, and lack microscale spatial resolution for localized treatments of PNI. In addition, characterization of these systems relies on wire connections to external equipment, or wireless integration that involves rigid, nondegradable modules that demands bulky postenclosures and thus compromises overall mechanical compliance.

The authors declare no competing interest.

This article is a PNAS Direct Submission.

[1]P.L., L.Z., and D.X. contributed equally to this work.

[2]To whom correspondence may be addressed. Email: ruili@dlut.edu.cn or sem@fudan.edu.cn.

This article contains supporting information online at https://www.pnas.org/lookup/suppl/doi:10.1073/pnas.2521817123/-/DCSupplemental.

Published January 9, 2026.

Alternative approaches based on photothermal therapy (PTT) and pharmacological delivery offer additional possibilities, particularly on the neural-tissue repair due to their high spatial precision for short-term/long-term in vivo therapy, in a minimally invasive, low toxicity, and biocompatible way (19, 20). Examples include flexible PTT implants that incorporate multilayer micro/nano-structures to yield tunable heating capability (37 to 45 °C) without tissue damages (21, 22), thereby enhancing the local blood flow, activating calcium ion channels and accelerating nerve regeneration (23, 24). Although promising in many scenarios, these and other techniques support single-mode operation, in most cases, which is only tailored for a specific region of tissues/organs for a single use (25). Critical challenges are in the development of miniaturized, wireless systems, in bioresorbable 3D forms, that can not only establish seamless interface adaptive to complex surfaces of peripheral nerves, but also provide multimodal operation [e.g., chemical (26), optical (27), mechanical (28), etc.] for dynamic modulation of PNI at different timescales.

For these purposes, this article reports a miniature, self-wrapping bistable (SWB) system as stable neural interface that enables 3D adaptation across localized region of PNI at various scales (from micrometer to millimeter level), and supports wireless, continuous multimodal treatments through PTT and drug delivery. These systems integrate multilayer structure that consists of 1) bilayers of silicon nitride (SiN_x, ~1 μm thick) as the outer substrate that self-wraps across the peripheral nerves (29, 30), 2) middle MXene-based layer (110 nm thick) that enables tunable PTT via near-infrared light (31, 32), and 3) inner drug layers (200 nm thick) that allow for pharmacological delivery. Such implant is fully biodegradable after assisting in vivo nerve repair, capable of providing wireless treatments at high spatiotemporal resolution during healing process. Experimental and theoretical results reveal that the platform can be mechanically triggered for self-driven 3D wrapping, at a range of diameters that spans from tens of micrometers (15 μm) to millimeters (1 mm), in a controllable way by adjusting SiN_x layer thickness. The following describes the multimodal treatments, with a focus on the combination of transient drug release and long-term photothermal stimulation. In vivo experiments in living rat models show that the well-established SWB neural interface can intimately integrate with the injured peripheral nerve and yield multifunctional stimulation as the combined therapy over months, in a bioresorbable design of stable implants for operation. Further ex vivo and in vitro assessments analyze the drug-photothermal synergy mechanism, the excellent biocompatibility and dissolving behavior during chronic use, suggesting the potential applications of importance for localized treatments of PNI for clinical medicine.

Results

Bioresorbable, Self-Wrapping Neural Interface for Wireless Peripheral Nerve Repair. Fig. 1*A* presents a schematic illustration of a representative platform, which is referred to as the SWB multimodal neural interface. The platform can be self-rolled up via mechanical triggers across the neuropathic injury regions at various spatial scales (from millimeters to micrometers), where external illumination of near-infrared light can generate localized heat for promotion of treatment process of nerve injury. Fig. 1*B* displays the layer stack that involves 1) a top layer with drug loading of sodium alginate (SA) and associated neural repair drugs [indole-3-propionic acid (IPA)] for short-term treatment (33), 2) a middle layer of the two-dimensional MXene photothermal materials that converts light to thermal energy to promote long-term, on-demand recovery, and 3) multilayer structures of SiN_x that drives the platform to wrap onto injured nerve region by internal stress. In this context, such platform is designed as fully bioresorbable implants, to avoid the secondary surgery for removal of the system that might induce additional risk.

The fabrication and transfer processes of the SWB system are depicted in *SI Appendix*, Fig. S1. Briefly, the SWB neural interface (SiN_x as the substrate layer) is directly deposited onto the handle $Ge/SiO_2/Si$ wafer (50 nm/300 nm/1 mm thick), subsequently released through sacrificial-layer etching and laser cutting techniques as the extended state and finally triggered to self-wrapping as the rolled-up state onto the dummy nerve. Fig. 1*C* demonstrates the mechanically bistable behavior of the dual-frequency SiN_x-based system, which adopts the idea from the pop-up ring. The first stable state, which refers to the extended state, represents the initial configuration before wrapping, with internal stress within the structure. By mechanical triggering of the SWB platform, the overall platform transitions from the extended state to the rolled-up state, thereby self-wrapping around the targeted nerve fiber. The finite element (FE) simulation shows the entire process of stable state transition. Specifically, the transition from the extended state to the rolled-up state occurs upon application of the mechanical stimulus, thus enabling the SWB to automatically envelop the entire surface of the target and ultimately achieving a stable mechanical state. Fig. 1*D* is the demonstrated concept that exhibits the entire process of the transition between the extended state and rolled-up state, with the target of a capillary fiber as the artificial nerve structure (diameter of 500 μm). The *Right Inset* of Fig. 1*D* shows the rolled-up state that intimately wraps across the body of artificial nerve fiber. Beyond the single self-rolling structure, Fig. 1*E* showcases the scalability of the fabrication of SWB neural interface system, into a large-scale array at extended states, distributed across planar silicon wafers.

Here, adjusting the thickness of the HF-SiN_x layers can vary the diameter of the rolled-up system, in a wide range from micrometer scales to millimeter scales. Fig. 1*F* presents the diameters of SWB neural interfaces as a function of the thickness of HF-SiN_x layers. For example, deposition of HF-SiN_x at 30 nm thickness yields to a highest resolution of SWB system with a rolling diameter of 15 μm compatible to those most sophisticated neural networks in human body (*SI Appendix*, Fig. S2), while a 1.5 μm thick HF-SiN_x layer corresponds to ~1 mm diameter of system that can couple with the large sciatic nerves, as shown in Fig. 1*G* and *SI Appendix*, Fig. S3. In addition, *SI Appendix*, Fig. S4 shows the FE simulations with different thicknesses of HF-SiN_x layers, well consistent with experimental results in Fig. 1*F*. Therefore, such controllable self-rolling characteristics can enable SWB neural interface with various scales, ranging from high resolution of the cellular level to large targets of macroscopic nerve systems. To validate the mechanical robustness of the SWB neural interface, we perform cyclic pressing-release experiments and FE simulations of the self-rolling SiN_x microtubes (diameter ≈ 0.8 mm). As shown in *SI Appendix*, Fig. S5*A*, the rolled tubes were repeatedly pressed and released over 100 cycles to simulate in vivo mechanical perturbations. The vertical diameter decreased from the initial D_0 to a minimum D_{min} during pressing and fully recovered to D_n after release. The nearly constant diameter recovery ratio ($\eta_D = D_n/D_0 \times 100\% \approx 100\%$) across 100 cycles (*SI Appendix*, Fig. S5*B*) indicates excellent elastic resilience and absence of fracture or plastic deformation. The FE results (*SI Appendix*, Fig. S5*C*) reveal a maximum principal strain of ~0.14% in the SiN_x bilayer, which is well below the reported fracture strain (~0.75%) (34). These results confirm that the SWB architecture operates well within the safe deformation range of the material and can withstand cyclic mechanical stress without structural damage. Therefore, the device maintains geometric integrity

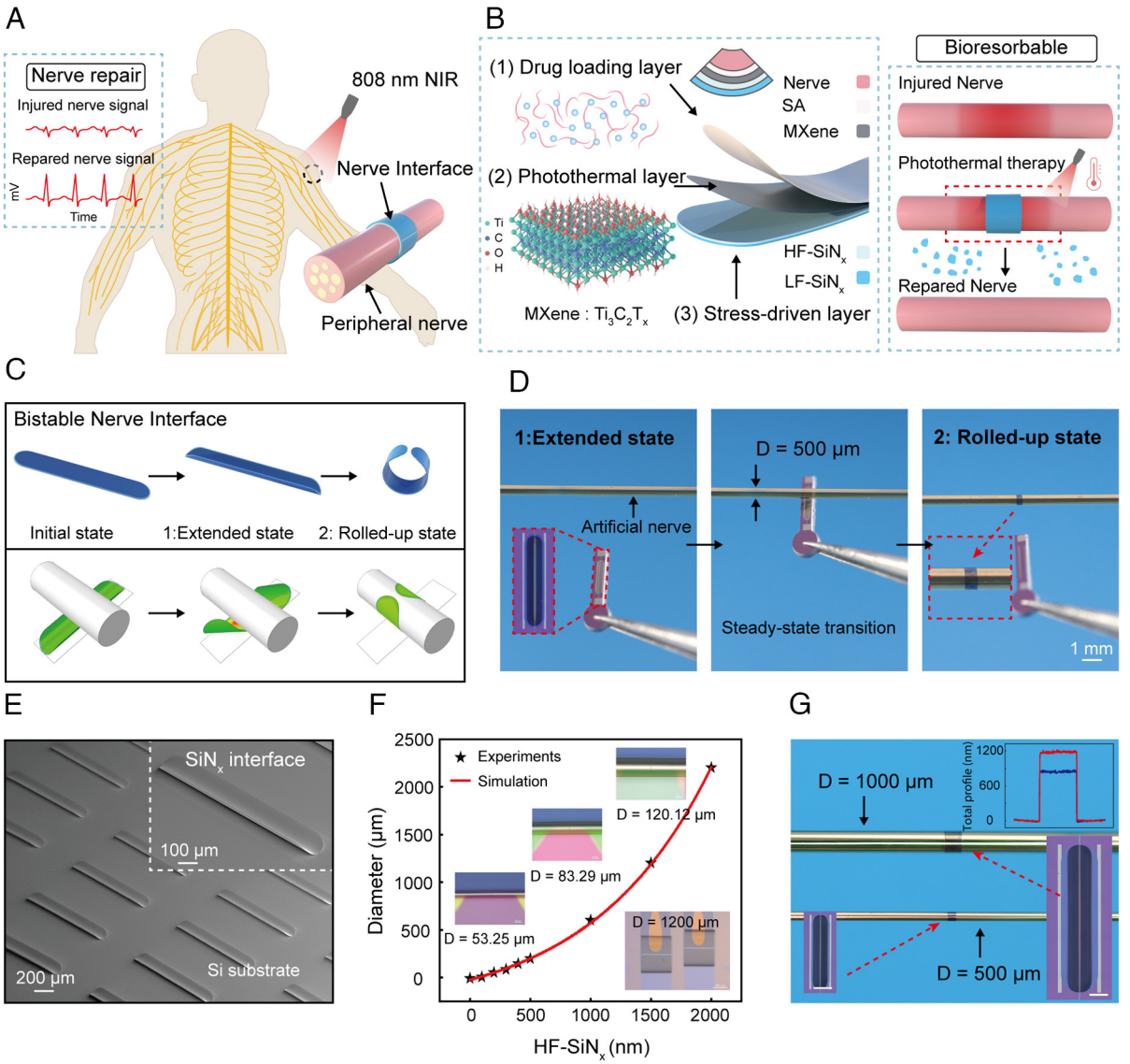

Fig. 1. Design, mechanism, and tunability of the SWB Neural Interface based on stress-gradient-induced transformation. (*A*) Schematic illustration of the SWB neural interface for peripheral nerve repair. (*B*) Exploded structural diagram showing the SWB neural interface's three-layer composition: 1) an inner SA layer loaded with IPA for early-stage neural repair drugs release; 2) a photothermal MXene layer ($Ti_3C_2T_x$) for long-term NIR activation; 3) a dual-frequency stress-driven SiN_x bilayer for self-wrapping actuation. (*C*) FE simulation and schematic of the SWB neural interface's bistable behavior. (*D*) Optical images showing the real-time wrapping process around an artificial nerve (D = 500 μm), from extended to rolled-up state. (*E*) SEM image of a SiN_x-based SWB neural interface array fabricated on a planar silicon substrate in the extended state. (*F*) Rolling diameter tunability as a function of HF-SiN_x thickness, ranging from ~15 μm to over 2 mm. (*G*) Demonstration of two SWB neural interfaces with different HF-SiN_x thicknesses conformally wrapping artificial nerves of 500 μm and 1 mm diameters, respectively; *Inset* shows profilometry confirming overall layer thickness.

and fatigue tolerance under implantation-relevant mechanical environments, ensuring reliable long-term operation.

FE Mechanical Analyses of SWB Neural Interface's Bistable Wrapping Behavior. As illustrated in Fig. 2*A*, the top (light blue) HF-SiN_x layer carries a positive internal stress, while the bottom (dark blue) LF-SiN_x layer is under negative internal stress. Detailed geometric parameters of the SWB neural interfaces are illustrated in *SI Appendix*, Figs. S6 and S7. Upon release from the prestressed condition, the HF-SiN_x/LF-SiN_x bilayer SWB neural interface transitions from the initial flat configuration to the extended state, and the resulting central angle, θ, in the extended state varies systematically with the design's aspect ratio, *L:W*. The detailed angle change curves are outlined in *SI Appendix*, Figs. S8 and S9. Both increasing L with constant W and increasing W with constant L produce a larger θ, i.e., tighter curvature, whereas decreasing either dimension yields a smaller θ, i.e., gentler bending. This geometrical control over θ enables precise tuning of the self-wrapping behavior of the SWB neural interface. Fig. 2*B* illustrates the thickness-dependent central angle tuning under *L:W* = 3:1. The upper graph plots θ in the extended state as a function of HF-SiN_x layer thickness (with LF-SiN_x layer thickness fixed at 40 nm), comparing FE simulations (red line) and experimental measurements (blue stars). Detailed FE simulation setups are described in *SI Appendix*, *Text S2*. As the HF-SiN_x thickness increases from 800 nm to 1,300 nm, θ decreases monotonically from ~300° to ~150°, indicating a systematic reduction in the bending moment due to the diminishing stress mismatch. Below the upper graph, two representative designs with the HF-SiN_x thicknesses ~900 nm (Design I) and ~1,200 nm (Design II) are further highlighted, corresponding to a central angle of ~240° and ~150°, respectively. Specifically, the upper panels show optical

images of partially rolled neural interfaces for Design I and II; the lower panels present corresponding simulated displacement contour maps. The close overlap of experimental outlines and simulated contour maps confirms the simulation accuracy and demonstrates precise, thickness-controlled tuning of self-wrapping behavior. *SI Appendix*, Fig. S10 further confirms the central angle change with the neural interface layer thickness.

Fig. 2*C* illustrates the strain-driven self-wrapping behavior. The FE contour maps of the principal strain ε in the extended state and the subsequent configurations are shown for Design I (upper figures, $\theta \sim 240°$) and Design II (lower figures, $\theta \sim 150°$). In Design I, a large strain mismatch (with ε spanning from −2 to 2%) concentrates strain into the edge "hot spots"; thus, under further mechanical stimulation, the extended state remains trapped in a collapsed, nonrolling shape. In Design II, by contrast, a smooth distribution of strain (ε spanning from −1.4 to 1%) enables the strain energy to accumulate uniformly across the bilayer SWB neural interface; once the snap-through threshold is reached, the stored energy is released to drive a rapid curvature inversion into a rolled-up state, where symmetric tension-compression domains stabilize the SWB neural interface. Fig. 2*D* illustrates the SWB neural interface deformation procedure from the extended state to the rolled-up state. Upon release, the SWB neural interface initially adopts the extended state. As the internal stress-driven bending moment accumulates, the curvature increases progressively, inducing localized midspan bending and partial wrapping. Once the stored bending energy overcomes the snap-through barrier, the SWB neural interface transitions abruptly into the rolled-up state. The upper optical images and the lower FE displacement contour maps, captured at successive release steps, demonstrate excellent agreement, both capturing the bistable rolled-up process. *SI Appendix,* Fig. S11 further elucidates the internal stress that contributes to the formation of the bistable transition. Upon relaxation to the extended state, the stress in the width direction is largely released while that in the length direction persists, and this residual stress supplies the elastic energy for the subsequent snap-through into the rolled-up state. To ensure conformal attachment without excessive compression or sliding along the nerve, the device's wrapping diameter (D_{wrap}) is always slightly smaller than the nerve diameter (D_{nerve}) as shown in *SI Appendix*, Fig. S12*A*. FE simulations further demonstrate that the maximum contact pressure exerted by the interface is 3.781 kPa, well below the conduction-block threshold (35, 36), as illustrated in *SI Appendix*, Fig. S12*B*. It is noted that this level of force, as illustrated in *SI Appendix*, Fig. S13, is much lower than the pressure from human gentle finger pressing (typically 30 to 200 kPa) (37, 38). Therefore, the nerve contact force during implantation is sufficient to trigger self-bending without causing excessive compression.

Fig. 2*E* illustrates the strain energy evolution during the autonomous nerve wrapping procedure under minimal mechanical stimulation. The plot shows how the total strain energy in the SWB neural interface evolves as a normalized loading Step is applied for Design I (red curve) and Design II (blue curve). In both designs, the external loading does work on the bilayer, steadily increasing the strain energy as the SWB neural interface bends. In Design I, the strain energy exhibits an initial increase, a subsequent drop, and a secondary increase without stabilization, indicating that the bending energy never exceeds the snap-through energy barrier; the structure remains trapped in the extended state without rolling. In Design II, by contrast, the energy curve reaches a maximum at the critical loading step, and this peak corresponds to the system reaching the snap-through energy barrier. Beyond this point, a rapid drop in the strain energy marks the snap-through transition, during which the stored bending energy is released to drive the SWB neural interface into the rolled-up state. The initial contact, snap-through onset, and fully rolled configurations are also illustrated. Fig. 2*F* illustrates the maximum-stress evolution under external loading. The plot traces the maximum principal stress σ_{max} in the bilayer as a function of the normalized loading step for Design I and II, with FE stress contour maps shown alongside. In Design I, σ_{max} sharply increases and then undergoes a minor decrease, followed by fluctuation, but fails to stabilize, reaching ~14.4 GPa in the HF-SiN_x layer, reflecting the neural interface collapse in its extended configuration. In Design II, conversely, σ_{max} climbs more slowly, peaking at ~4.4 GPa where the stored bending energy reaches the energy barrier for snap-through. At this critical stress, the SWB neural interface starts a transition into the rolled-up state, and σ_{max} drops as the released bending energy redistributes stresses evenly around the cylinder shape.

PTT and Drug Release for Neural Treatments. To endow the SWB multimodal neural interface with light-controlled treatments, a photothermally responsive $Ti_3C_2T_x$ MXene layer is deposited on the SiN_x substrate. Fig. 3*A* shows the optical images of the platform at the initial flat configuration before self-rolling, with multilayer structures of SiN_x (1 μm) and MXene materials (110 nm), respectively. Here, the MXene layer is synthesized via a selective etching process using hydrochloric acid and lithium fluoride, as illustrated in *SI Appendix*, Fig. S14. The results of X-ray diffraction (XRD) and Raman spectroscopy confirm the effective removal of the aluminum layers and the successful formation of multilayer or few-layer MXene nanosheets (*SI Appendix*, Fig. S15). The layered morphology observed in scanning electron microscopy (SEM, Fig. 3 *B*, *Inset*) further validates the successful synthesis. The ultraviolet (UV)-visible absorption spectrum (Fig. 3*B*) exhibits a strong absorption peak at the NIR region (808 nm of the laser wavelength as an example), suggesting the excellent photothermal conversion capability of MXene.

For preliminary evaluation, the MXene nanolayer exhibits repeatable heating–cooling cycles with good photothermal stability under NIR illumination, as shown in Fig. 3*C*. Specifically, the power density of 125 mW/cm^2 corresponds to the temperature increase up to over 10 °C, yielding a rapid responsive time of 30 s. Infrared thermal imaging under laser excitation is shown in *SI Appendix,* Fig. S16. Overall, the photothermal performance of the SWB neural interface highly depends on the MXene film dimensions such as the material thicknesses, lateral areas, and input laser power density (*SI Appendix*, Fig. S17). In order to ensure the efficient photothermal effect, we evaluate the NIR light transmittance of SiN_x layer (Fig. 3*D*). Here, as a rolled-up state, the laser illuminates the 3D construction at the vertical direction, as displayed in the *Inset* of Fig. 3*D*. Results of the transmission spectrum of the SiN_x membrane yield a NIR transparency of ~90% at NIR illumination, indicating excellent light transmittance particularly at NIR region to allow for efficient photothermal conversion of the underlying MXene layer.

As a demonstrated example, Fig. 3*E* compares the temperature rise under different laser power densities with and without MXene layers coated, both as a self-rolling diameter of the SWB neural interface platform as 500 μm (details appear in *SI Appendix*, Figs. S18 and S19). These results reveal that the MXene-enhanced SWB neural interface achieves up to 288% improvement photothermal response with a relative increase of temperature treatments of ~15 °C. Fig. 3*F* shows a heat map of the surface temperature of the SWB neural interfaces after rolled up at varying power levels that range from 100 mW/cm^2 to 150 mW/cm^2, and at illumination durations that range from 0 s to 10 s. Specifically, the top

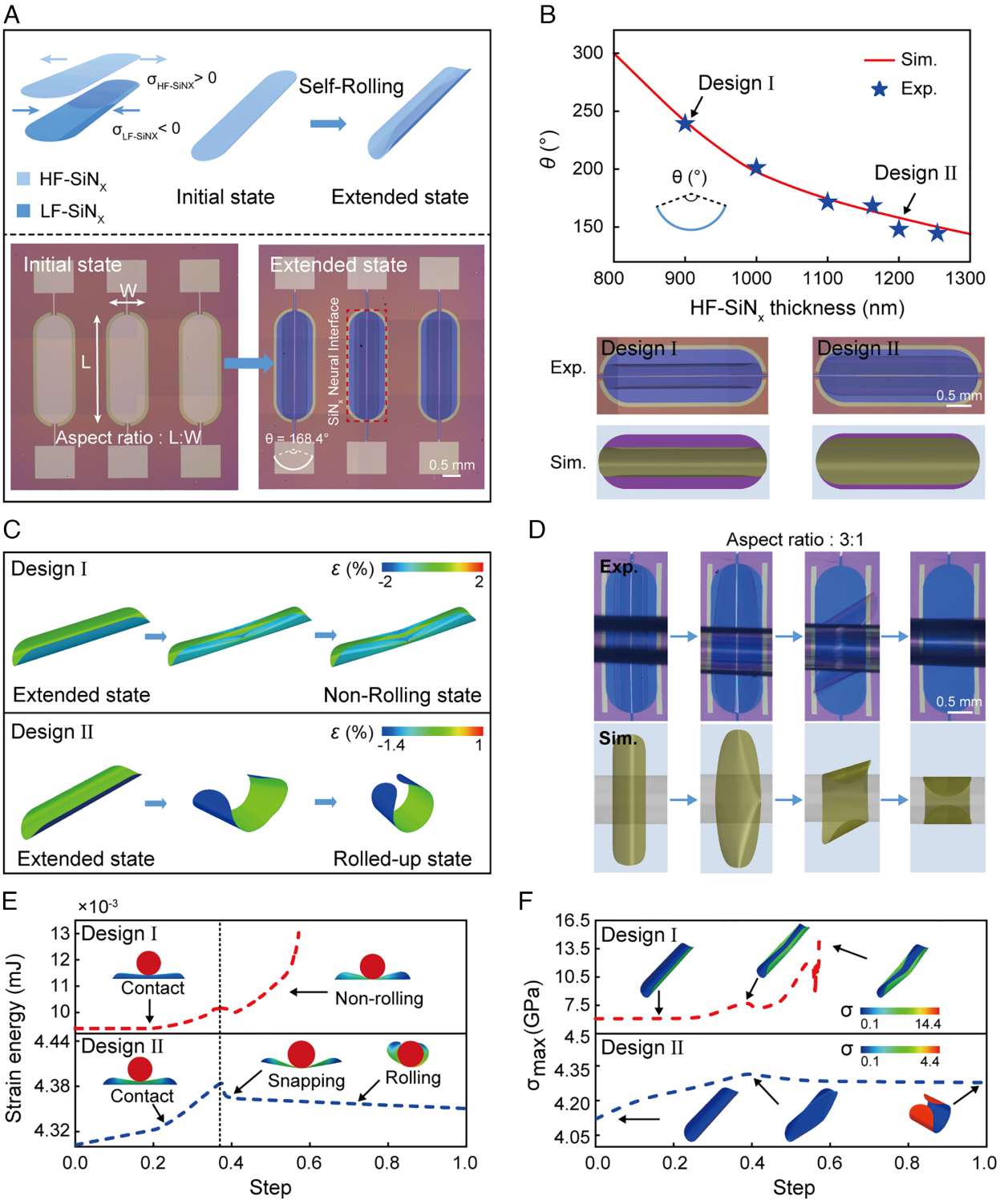

Fig. 2. Mechanical analyses of the neural interface's bistable wrapping behavior based on the FE simulation. (*A*) Schematic illustration of the transition procedure of the HF-SiN_x/LF-SiN_x bilayer SWB neural interface from the initial state to the extended state. B) Central angle θ vs. HF-SiN_x thickness (800 to 1,300 nm) under L:W = 3:1. Design I (~900 nm) and II (~1,200 nm) are highlighted, with experimental snapshots and FE displacement contours showing excellent agreement. (*C*) Strain-driven self-wrapping behavior. In Design I, a large strain mismatch localizes strain at edge hot spots, trapping the bilayer SWB neural interface in a collapsed, nonrolling state. In Design II, uniform strain and stored energy triggers snap-through into a rolled-up state. (*D*) Deformation procedure of the SWB neural interface from the extended state to the progressive bending and partial rolled-up state, finally transiting to the rolled-up state. Experimental snapshots and FE displacement contours show excellent agreement. (*E*) Strain energy evolution under minimal mechanical stimulation: in Design I, the energy increases, then decreases, and subsequently increases again without stabilization, indicating nonrolling deformation procedure; in Design II, the energy peaks and then drops, indicating a snap-through that releases stored energy and enables rolling. (*F*) Maximum stress (σ_{max}) evolution under minimal mechanical stimulation: Design I exhibits higher and nonuniform stress distributions, peaking at σ_{max} ~ 14.4 GPa, whereas Design II shows lower, more uniform and stable stress levels around σ_{max} ~ 4.4 GPa.

surface of the targeted structure at rolled-up state shows a wide range of temperature rise across tunable illumination durations and power densities, yielding efficient PTT with different heating treatments from room temperature to even 50 °C. As a consequence, Fig. 3*G* presents a set of infrared thermal images using a commercial infrared camera across a broad scope of spatiotemporal

scales, results of which demonstrate the use of MXene-based neural interface can effectively enable localized temperature rise at a spatial resolution of submillimeter level (from hundreds of micrometers to millimeters, the length of the microtubes).

To further ensure effective and controllable PTT under physiological conditions, we conduct additional tissue-penetration and photothermal experiments using porcine-skin models (as shown in *SI Appendix*, Fig. S20). The attenuation of 808 nm NIR light through biological tissue was quantified across 0 to 12.5 mm thicknesses (*SI Appendix*, Fig. S20 *A* and *B*), showing an exponential decay of transmitted intensity with an overall attenuation coefficient $\mu \approx 0.503\ mm^{-1}$, consistent with the Beer–Lambert law that describes optical propagation in biological tissues (39, 40):

$$I = I_0 e^{-\mu d},$$

where d is the tissue thickness, μ is the attenuation coefficient, I_0 is the initial light intensity, I is the intensity of light after the attenuation. At a representative tissue thickness of 5 mm (comparable to the skin-to-nerve depth in rodent models) the transmitted intensity retained ~6.7% of the incident light, which was sufficient to induce a ~6 °C temperature rise on the MXene-coated SWB interface (*SI Appendix*, Fig. S20*C*). Furthermore, under a simulated physiological environment (T_0 = 37.3 °C), photothermal heating through 5 mm-thick tissue layers achieved a steady-state temperature of 43 °C at a laser power density of 730 mW/cm^2 (*SI Appendix*, Fig. S20 *D* and *E*). This temperature corresponds to the optimal therapeutic range reported for promoting neural regeneration (41–43) and remains below the ANSI Z136.1-2007 safety limit for skin exposure. These results confirm that the MXene–SWB interface can achieve physiologically compatible and spatially confined heating for effective in vivo photothermal neuromodulation.

Besides the photothermal treatments, drug delivery released through the rolled-up state is of critical importance to injured neural-tissue recovery. As an example, the drug-based composite, rhodamine B(RB) mixed with SA, forms on the multilayers of SiN_x-MXene via spin-coating methods. As shown in *SI Appendix*, Fig. S21, the over structure comprises 1 μm thick SiN_x layer, 110 nm thick MXene layer, and 200 nm thick SA-RB layer. The optical images and the fluorescence image of the SWB neural interfaces at various states (the initial flat configuration and the extended state) appear in Fig. 3*H*, corresponding to the 3D self-wrapping with drug loading in a 3D structure. To evaluate therapeutic drug release, the neurorepair drug IPA is incorporated into the SA layer. Fig. 3*I* displays the UV–vis absorption spectra of IPA of the trilayer structure at extended state at various concentrations ranging from 10 to 50 μg/mL, all with a distinct peak at 280 nm upon immersing in 2 mL deionized water. In this context, Fig. 3*J* extracts the different absorption peaks as a function of drug concentrations, where the results yield a linear calibration curve (R^2 = 0.99) for quantitative analysis. In vitro measurements of such structure at rolled-up 3D state in Fig. 3*K* shows an absorption peak also at 280 nm, consistent with the results of the extended state in Fig. 3*I*. The calculated release amount of the drug composite is ~41.7 μg that can enable sufficient nerve recovery, validating the drug delivery from the SWB neural interface for neural tissue treatments (*Inset* of Fig. 3*K*).

To further elucidate the time-dependent drug-release behavior and kinetics, we perform additional in vitro experiments using IPA as a neuroprotective model drug loaded within the SA carrier (*SI Appendix*, Fig. S22). The IPA-loaded SWB neural interfaces are immersed in phosphate-buffered saline (PBS, pH 7.4, 37 °C), and aliquots are collected every 15 min for quantification by UV–vis absorption at 280 nm. The spectra in *SI Appendix*, Fig. S22*B* exhibit a characteristic IPA absorption peak whose intensity increases over time, indicating sustained diffusion into the medium. The cumulative release profile (*SI Appendix*, Fig. S22*C*) reveals that ~80% of IPA is released within 45 min, followed by a slower release phase approaching the saturation at around 120 min. We further analyze the cumulative release data using classical kinetic models to quantitatively elucidate the underlying release mechanism (44, 45). As an example, the Weibull model is expressed as:

$$F(t) = 1 - \exp[1 - (\frac{t}{\lambda})^{\beta}],$$

where F(t) represents the fractional release, λ is the characteristic time constant, and β denotes the shape parameter associated with the release mechanism (46, 47). These findings demonstrate that the SWB neural interface provides an efficient and controllable drug delivery process under physiological conditions, enabling reliable short-term pharmacological treatment that complements long-term photothermal modulation.

SWB-Assisted Treatment of the Sciatic Nerve Repair for Motor Function Recovery. To evaluate the potential of the developed SWB neural interface for the implantable therapy, we establish a sciatic nerve crush injury model in 6-wk-old male Sprague-Dawley (SD) rats. Fig. 4*A* illustrates a schematic of the SWB neural interface encapsulating the injured sciatic nerve, with NIR light irradiation enabling assisted photothermal repair. Fig. 4*B* presents intraoperative images of the three experimental groups: the sham group (healthy control with uninjured sciatic nerve), the model group (crushed sciatic nerve with no intervention), and the SWB-treatment group (crushed sciatic nerve wrapped with the SWB neural interface for assisted repair).

During the wrapping treatments, we apply NIR laser irradiation at 808 nm with a power density of 730 mW/cm^2 twice per week, with each session lasting 5 min. As such, the functional and histological analyses characterize the extent of the localized nerve repair after 4-wk postoperation. Fig. 4*C* shows representative walking track images from the three groups, these images serve to calculate the sciatic functional index (SFI) and evaluate the extent of the locomotor recovery (48). *SI Appendix*, Fig. S23 illustrates the calculation method of the SFI and the procedure for acquiring footprint images. As a result, the calculated values of SFI reveal that the implantation of the SWB neural interfaces can reduce the motor-function impairment, with a higher SFI score that is comparable to those of sham group. Specifically, the SWB-treatment group exhibits significantly improved SFI scores (−19.0 ± 1.2) compared to the untreated model group (−38.2 ± 2.5), approaching to those of sham group (−2.1 ± 1.5), as summarized in Fig. 4*D*. Fig. 4*E* displays representative gastrocnemius muscle images from each group, with the left and right muscles in each image corresponding to the gastrocnemius muscles of the left and right hindlimbs of the rat, respectively. Fig. 4*F* presents the results of quantitative analysis of the muscle wet-weight ratio (injured side vs. contralateral side) in the SWB-treatment group (84.2 ± 2.1%) that is compatible to that of sham group (98.4 ± 4.3%), which are both notably higher than that in the model group (38.5 ± 1.7%). These findings indicate that SWB-assisted repair effectively mitigates muscle atrophy via drug delivery and photothermal treatments.

To further assess the electrophysiological recovery of injured sciatic nerve, we measure the compound muscle action potentials (CMAP) as described in *SI Appendix*, Fig. S24. Fig. 4*G* shows the evoked CMAP of the gastrocnemius muscle in each group (sham group, model group, and SWB-treatment group), all of which are under an applied identical electrical stimulation (0.7 mA, 5 ms pulse width, 10 Hz) on the proximal segment of the sciatic nerve. Fig. 4*H* collects and quantifies the peak amplitudes of CMAP in

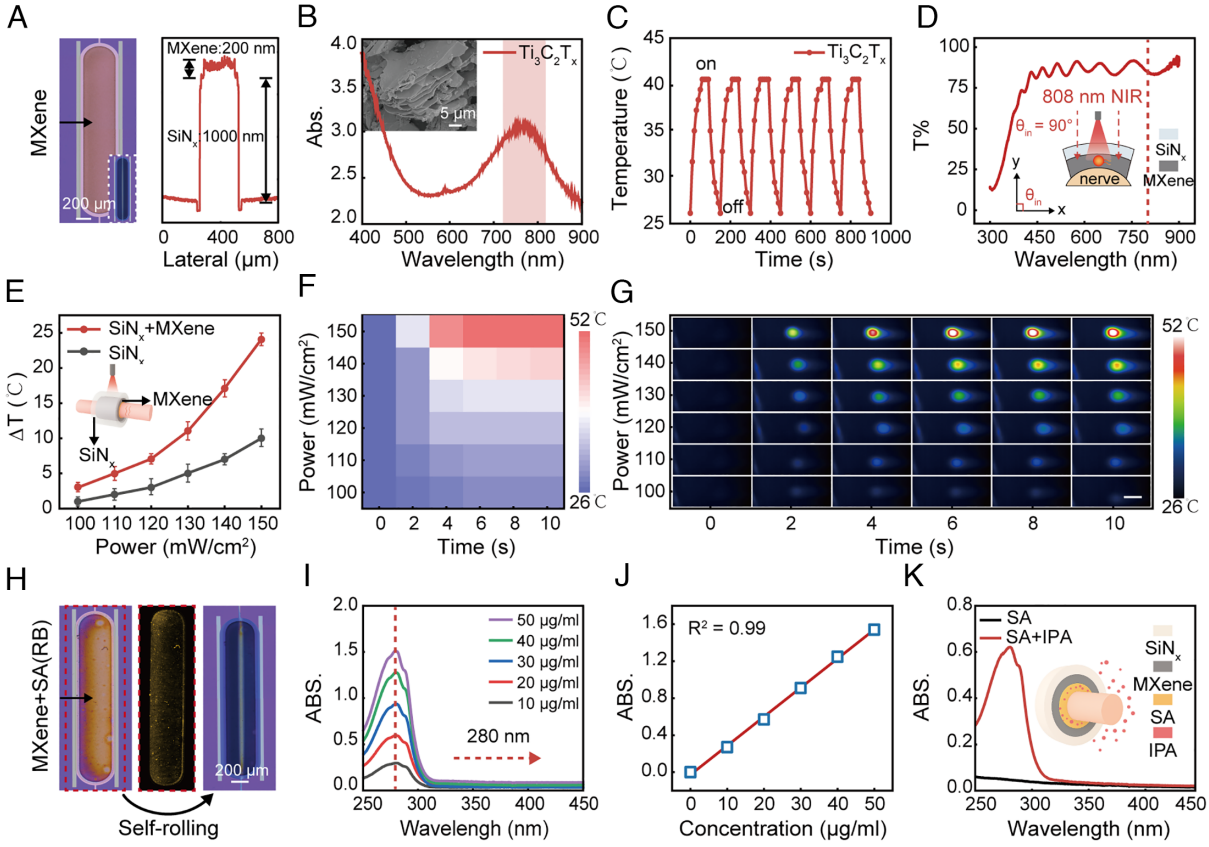

Fig. 3. Characterization of MXene-based photothermal and drug-release functionalities in the SWB neural interface. (*A*) Optical image (*Left*) and step profiler measurement (*Right*) of the SWB neural interface composed of a 1,000 nm SiN_x substrate and a 110 nm $Ti_3C_2T_x$ MXene layer; *Inset*: optical image of the extended state structure after sacrificial layer release. (*B*) UV–vis absorption spectrum of MXene; *Inset*: SEM image of multilayered MXene. (*C*) Photothermal cycling performance of MXene film under 808 nm laser irradiation. (*D*) Transmission spectrum of the SiN_x membrane indicating ~90% NIR transparency at 808 nm; *Inset*: schematic showing normal-incidence NIR penetration through SiN_x. (*E*) Comparison of temperature increase (ΔT) between SiN_x and SiN_x-MXene neural interface under different laser powers; *Inset*: experimental configuration illustration. (*F*) Heatmap of SiN_x-MXene neural interface under various laser powers (100 to 150 mW/cm^2) and durations (0 to 10 s). (*G*) Infrared thermal images of MXene-coated neural interface at different time points and laser powers, with peak temperature reaching ~52 °C. The scale bar represents 1 mm. (*H*) Optical (*Left* and *Right*) and fluorescence (*Center*) images of a trilayer SWB neural interface (SiN_x/MXene/SA-RB). (*I*) UV–vis absorption spectra of IPA at different concentrations; the peak at 280 nm is used for quantification. (*J*) Linear calibration curve of IPA absorbance at 280 nm (R^2 = 0.99). (*K*) UV–vis spectra of inner drug layer solutions from SA– and SA+IPA-loaded neural interface after immersion; *Inset* shows IPA release from the nerve-facing side.

each group: 2.1 ± 0.03 mV for the sham group, 1.4 ± 0.02 mV for the model group, and 1.7 ± 0.02 mV for the SWB group, indicating improved nerve conduction in the SWB group. Fig. 4*I* shows representative toluidine blue-stained cross-sections of sciatic nerves from the three groups at 30 d postsurgery. Based on these stained images, we can perform quantitative analysis of nerve fiber parameters, such as myelin sheath thickness and G-ratio. As shown in Fig. 4*J*, the average myelin sheath thickness in the SWB group (1.65 ± 0.21 μm) is significantly greater than that in the model group (1.23 ± 0.18 μm), and slightly lower than that in the sham group (1.82 ± 0.22 μm). The G-ratio, defined as the axon diameter divided by the total fiber diameter, serves as a key index of myelination. As shown in Fig. 4*K*, the average G-ratio is 0.33 ± 0.12 in the sham group, 0.37 ± 0.12 in the model group, and 0.36 ± 0.16 in the SWB group, respectively. Additional morphometric analysis (*SI Appendix*, Fig. S25) confirms that the SWB group exhibits increased myelinated axon area and total fiber area. These results collectively demonstrate that the SWB neural interface facilitates peripheral nerve repair by promoting axonal regrowth, remyelination, and functional restoration.

To clarify the contributions of photothermal stimulation and pharmacological delivery to neural repair, we conduct additional in vivo experiments using a rat sciatic-nerve crush model with four treatment groups: Control (no intervention), Drug (SWB cuff loaded with IPA drug only), PT (SWB cuff containing MXene for PTT), and PT + Drug (dual-functional SWB cuff integrating both modalities), as shown in *SI Appendix*, Fig. S26*A*. The footprint and SFI analyses (*SI Appendix*, Fig. S26 *B–D*) demonstrate various recovery effects in all treatment groups compared to the control group, with the PT + Drug group exhibiting the most pronounced improvement (SFI = −26.7 ± 1.2 vs. −92.5 ± 2.5 for control at day 15). In addition, the gastrocnemius muscle recovery (*SI Appendix*, Fig. S26 *E* and *F*) further confirms this trend: the wet-weight ratio of the injured side reached 72.0 ± 2.1% in the PT + Drug group, which is significantly higher than those of the control (46.8 ± 1.7%) Drug (52.4 ± 2.3%), and PT (57.6 ± 2.0%) groups ($P < 0.01$). These results indicate that both photothermal stimulation and drug release can promote nerve regeneration by different effects, and the combination of these two therapies together yields the most significant improvement.

Mechanistically, the drug therapy acts immediately after implantation: the inner IPA layer contacts neural tissue and activates the pregnane X receptor (PXR) pathway to modulate the immune microenvironment, enhancing neutrophil recruitment and early axonal regrowth (33). Meanwhile, photothermal stimulation (43 °C) from the MXene layer under 808 nm NIR light activates calcium channels in Schwann-cell membranes, facilitating angiogenesis and remyelination (26). The combined treatment provides

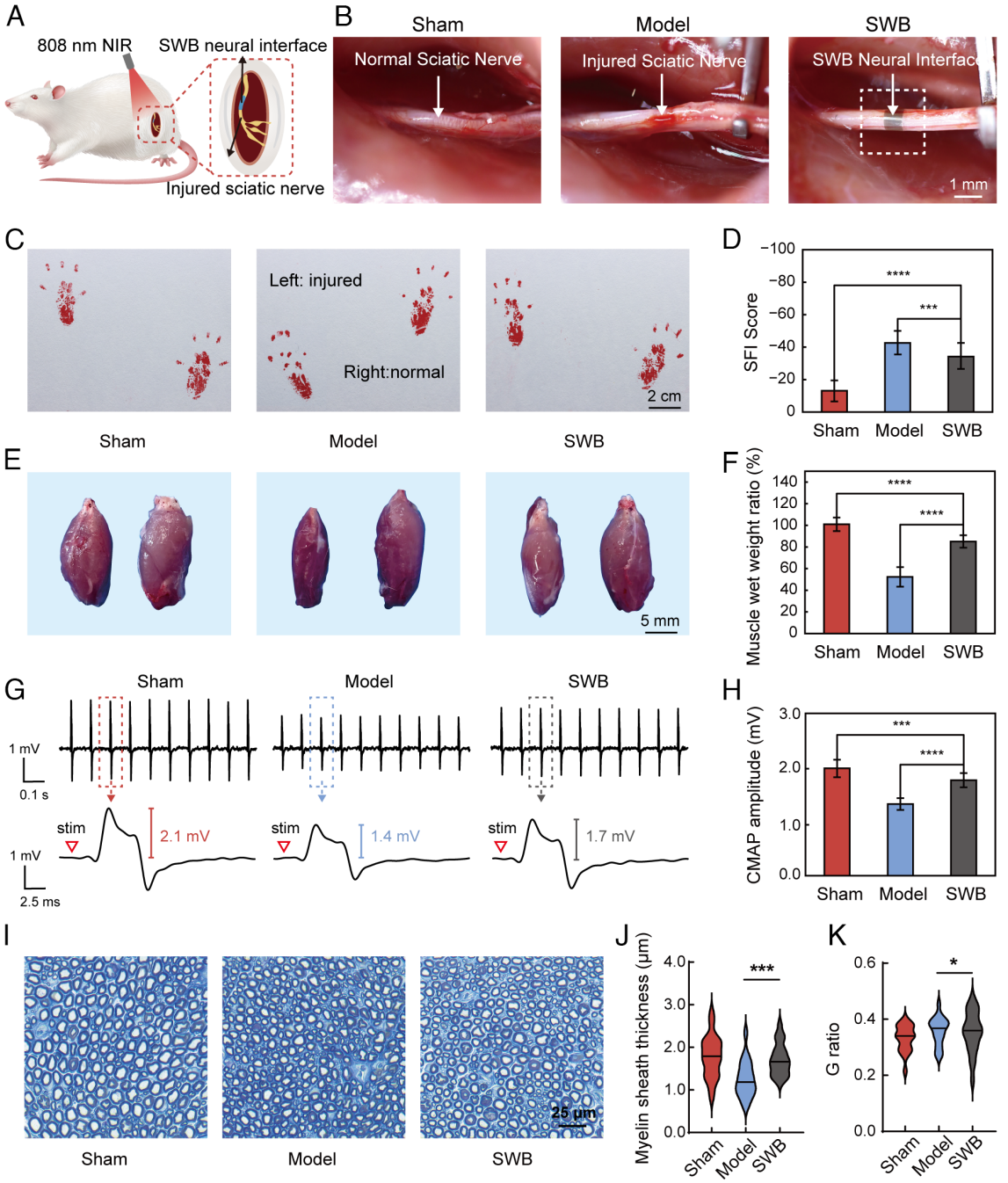

Fig. 4. Evaluation of functional recovery in a rat sciatic nerve crush injury model treated with the SWB neural interface. (*A*) Schematic illustration of the NIR-triggered photothermal modulation applied to the SWB-wrapped sciatic nerve. (*B*) Intraoperative images of the three groups: Sham (no injury), Model (crush injury with natural recovery), and SWB (crush injury treated with SiN_x-based SWB neural interface). (*C*) Representative SFI footprints obtained using walking track analysis. (*D*) Quantitative SFI scores (n = 5 per group). (*E*) Representative images of bilateral gastrocnemius muscles from each group at 4 wk. (*Left*: postoperative muscle tissue; *Right*: normal muscle tissue). (*F*) Quantification of gastrocnemius muscle wet weight ratio (injured vs. contralateral leg). (*G*) CMAP elicited from the sciatic nerve and corresponding signal waveforms. (*H*) Quantification of CMAP amplitudes. (*I*) Toluidine blue-stained cross sections of regenerated sciatic nerves at 4 wk. (*J* and *K*) Quantitative analysis of myelin sheath thickness (*J*) and G-ratio (*K*) derived from semithin sections. All quantitative data are expressed as the means ± SEMs. Asterisks indicate statistically significant comparisons determined by Student's *t* test as follows: **P* < 0.05, ***P* < 0.01, ****P* < 0.001, and *****P* < 0.0001.

early-phase immune modulation and later-phase remote photothermal activation, resulting in spatial-temporal synergy that markedly accelerates nerve regeneration and functional recovery (3, 4).

Bioresorbability and Chronic Biocompatibility Assessments of the SWB Neural Interface. As a key feature of the implantable electronics, an ideal neural interface can be fully dissolvable by hydrolysis behavior after stable operation in vivo, which can avoid the need for secondary surgical removal. Fig. 5*A* highlights the experimental setup for evaluating the processes of dissolution of a representative SWB neural interface during soaking in phosphate-buffered saline (PBS, pH 7.4) solution at 95 °C, in an accelerated manner (~18 times relative to body temperature) according the Arrhenius scaling equation (49, 50). Following results show a set of optical images at various time points during immersion at the elevated temperature (95 °C). Here, the constituent materials of the system (SiN_x/MXene) exhibit excellent bioresorbability during long-term immersion in biofluids (32, 51). As a demonstration, the ultrathin layer of MXene delaminates from

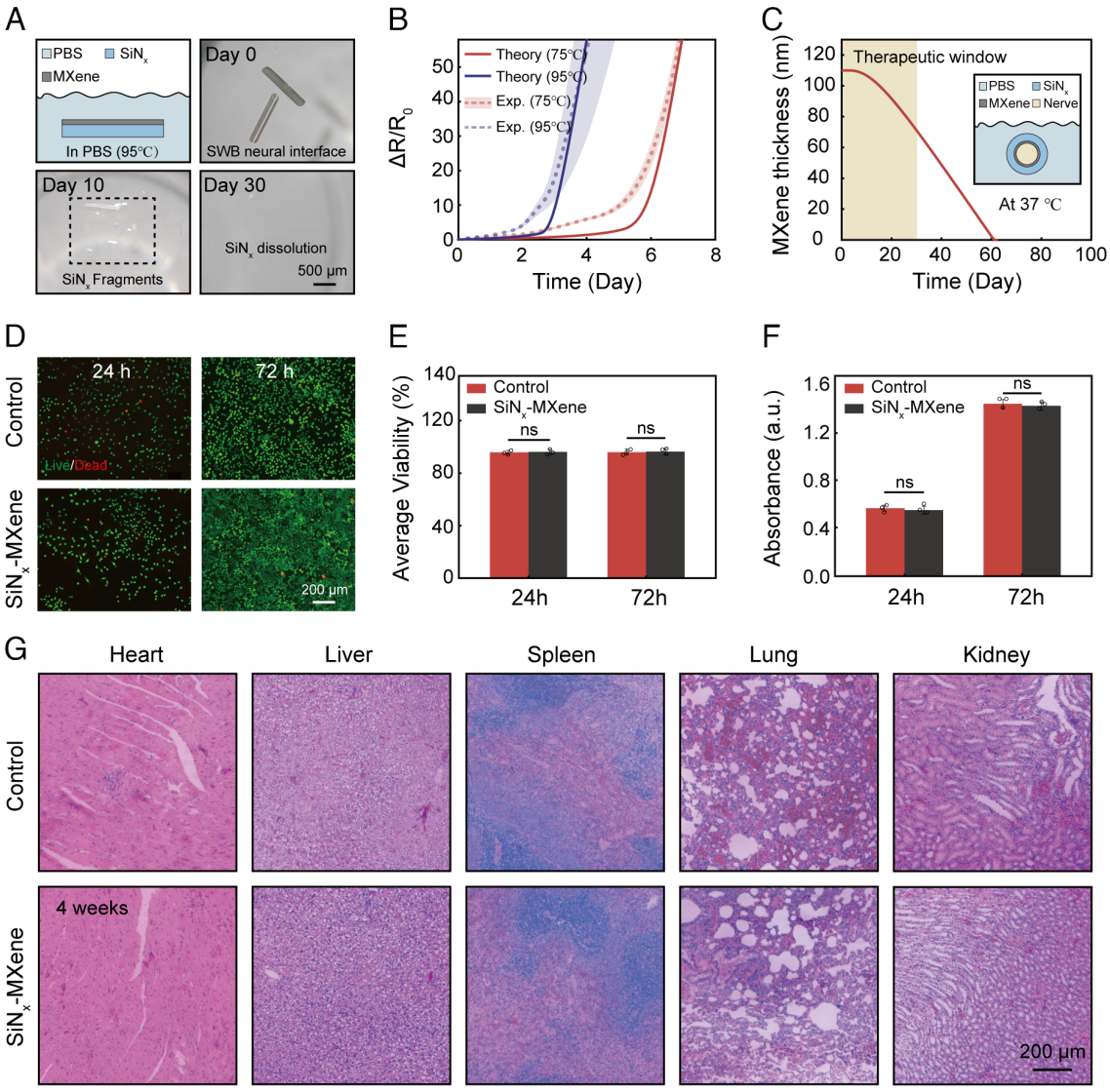

Fig. 5. Bioabsorbability and biocompatibility evaluation of the SiN_x-MXene-based SWB neural interface. (*A*) Optical images of the SWB device immersed in 95 °C PBS over 30 d. (*B*) Time-dependent change in surface resistance ($\Delta R/R_0$) of MXene during immersion at 75 °C and 95 °C, showing experimental data and theoretical predictions. (*C*) Theoretical simulation of MXene degradation within the SWB neural interface under physiological conditions. (*D*) Photographs of the L929 cells using Live and dead cell staining method with(out) the SWB nerve interface leaching liquid culturing for 24 and 72 h. (*E*) Average viability of L929 cells in control group and SWB nerve interface group after incubation period of 24 and 72 h. (*F*) Absorbance of L929 cells in CCK-8 assay cultured with and without SWB leaching liquid. Error bars correspond to the SD for three independent measurements. ns represents no significant difference ($P > 0.05$). (*G*) Representative histology images with H&E staining of cross-sectional areas of the heart, lung, kidney, spleen, and liver of rats without (control group, first row) and with a SWB nerve interface after 4 wk (experimental group, second row) of implantation (n = 3 animals per group over three independent experiments).

the SiN_x substrates at Day 10, and simultaneously the SiN_x-based microtube structure loses their shapes and fully dissolves during the soak test after 1 mo, with dissolution rates consistent with those reported in previous literatures (52).

Considering that the MXene photothermal layer serves as the primary functional component of the SWB neural interface, we systematically investigate its degradation behavior through both experimental studies and theoretical modeling. Fig. 5*B* presents both the experimental measurements (dots) and theoretical calculations (lines) of the time-dependent surface resistance of MXene immersed in PBS solutions at different temperatures. The normalized surface resistance ($\Delta R/R_0$) increases dramatically over days of soaking, where R_0 denotes the initial electrical resistances of MXene layer and ΔR corresponds to the variation of resistance during immersion. As an example, the results of $\Delta R/R_0$ at 75 °C sharply rise at Day 5, indicating rapid degradation of the MXene layer. Specifically, a single-layer reactive diffusion model applied to the surface resistance data yields the water diffusivity in the MXene layer, $D_{MXene} = 10^{-11-1709/T}$ cm^2 s^{-1}, and the reaction rate constant for hydrolysis, $K_{MXene} = 10^{2.2-1709/T}$ s^{-1}, where T is the absolute temperature. Details appear in *SI Appendix*, *Text S12*. Under physiological conditions (i.e., at body temperature of 37 °C), the theoretical model simulates the MXene layer's thickness via the bioresorbable behavior, as shown in Fig. 5*C*. The thickness initially decreases slowly from 110 nm over a brief period due to the barrier from SiN_x, and then continues to decrease at a steady rate due to substantial water penetration through SiN_x until the MXene layer is fully resorbed in biofluids after sufficient time.

To experimentally validate the bioresorbability of the MXene layer within the SiN_x-MXene SWB neural interface, we conduct accelerated degradation tests in PBS (pH 7.4) at 75 °C for 3 to 18 h, and monitor the elemental release using inductively coupled plasma optical emission spectrometry (ICP-OES) (*SI Appendix*, Fig. S27).

The Si and Ti concentrations, originating from the SiN_x and MXene components, respectively, increase progressively with immersion time and reach saturation after ≈ 12 h, indicating continuous hydrolysis and oxidation of the hybrid layers. These results confirm the gradual dissolution of both materials in aqueous physiological media. The degradation of MXene proceeds through two cooperative pathways (53): i) chemical oxidation–hydrolysis, in which water and oxygen oxidize $Ti_3C_2T_x$ edges into TiO_2 and amorphous carbon (54, 55), and ii) enzyme-mediated oxidative degradation, where reactive-oxygen-producing enzymes such as myeloperoxidase (MPO) catalyze further oxidation under biological conditions. In vivo, MPO-driven oxidation within macrophage lysosomes further accelerates degradation, yielding biocompatible metal oxides that can be metabolized and excreted (56). *Inset* of Fig. 5*C* shows a cross-sectional schematic of the degradation simulation. The results indicate that the MXene layer's lifetime significantly exceeds the 30-d treatment cycle, thereby ensuring continuous photothermal performance throughout the therapeutic window. The multilayer reactive diffusion model demonstrates that the SWB neural interface immersed in PBS at 95 °C fully dissolves within approximately 30 d (*SI Appendix*, Fig. S28), consistent with the experimental observations shown in Fig. 5*A*. We present the derivation procedures for both the single-layer and multilayer reactive diffusion models comprehensively in *SI Appendix*, *Text S13*.

To evaluate the biocompatibility of the SWB neural interface, we first conduct in vitro cell experiments. Here, we coincubate L929 fibroblasts with a 24-h leachate extracted from the SWB neural interface for 1 d and 3 d, using standard culture medium as the control. As shown in Fig. 5*D*, live/dead staining of the SiN_x-MXene group reveals no obvious abnormal cell death compared to the control. Quantitative analysis in Fig. 5*E* confirms that there is no statistically significant difference in cell viability between the SiN_x-MXene and control groups ($P > 0.05$, two-tailed unpaired t test; data presented as mean ± SD, n = 3). In addition, the result of CCK-8 assay in Fig. 5*F* shows a negligible difference in absorbance value between the two groups ($P > 0.05$), indicating the excellent cytocompatibility of the SWB neural interface. Organ toxicity assessment serves as another essential criterion for evaluating the biocompatibility of the SWB neural interface. We conduct hematoxylin and eosin (H&E) staining of major organs (heart, liver, spleen, lung, and kidney) from mice 4 wk after SWB neural interface implantation. Organs from healthy mice raised under the same conditions for 4 wk serve as the control. Fig. 5*G* shows that the SWB-implanted group exhibits no signs of inflammation, necrosis, or tissue architecture disruption compared to the control group. All the results above demonstrate that the SWB neural interface possesses excellent bioresorbability and biocompatibility both in vitro and in vivo.

Discussion

In summary, this work presents a miniature SWB neural interface integrating a dual-frequency SiN_x bilayer, MXene photothermal layer, and drug-loaded core for multimodal peripheral nerve therapy. The device achieves stable 3D, suture-free wrapping and delivers synergistic photothermal and pharmacological treatment with high spatiotemporal precision. In vivo studies confirm excellent biocompatibility, effective nerve repair, and complete bioresorption after functional recovery. Beyond photothermal modulation, the MXene layer also holds great promise for photoelectric stimulation, owing to its high electrical conductivity, broadband optical absorption, and rapid carrier dynamics (57). These features enable efficient conversion of light into localized electric fields, offering the potential for precise, light-controlled neuromodulation within a fully wireless and bioresorbable platform (58–60). Future efforts should focus on improving the long-term stability and tunable degradation kinetics of the SWB system under physiological conditions, while ensuring scalable fabrication and biomechanical adaptability for dynamic neural environments. Integration with signal acquisition and closed-loop control will further advance intelligent, implantable bioelectronics for precise and durable therapies across neural and vascular regeneration.

Materials and Methods

Cytotoxicity Evaluation. The SWB neural interface was sterilized by UV irradiation and cocultured with L929 mouse fibroblast cells (Procell Life Science & Technology Co., Ltd.) for 24 and 72 h in a constant-temperature incubator at 37 °C. After incubation, the cells were stained using a calcein acetoxymethyl/propidium iodide (Calcein-AM/PI) double-staining kit (BB-4126, BestBio) and incubated for 15 min at room temperature. A fluorescence microscope was used to capture images of live (green) and dead (red) cells. To assess relative cell viability, the cocultured cells were treated with culture medium containing 10% Cell Counting Kit-8 (CCK-8, IV08-100, Invigentech) and incubated for 2 h at 37 °C. The absorbance at 450 nm was measured using a microplate reader to quantify cell viability.

Statistical Analysis. All data were expressed as mean ± SD and analyzed using GraphPad Prism 9.3.1 (GraphPad Software, San Diego, CA). Image data were processed using ImageJ software. For comparisons between two groups, Student's t test was applied. For comparisons among multiple groups, one-way ANOVA followed by Tukey's post hoc test was used. Statistical significance was denoted as follows: $P < 0.05$ (*), $P < 0.01$ (**), $P < 0.001$ (***), $P < 0.0001$ (****), and ns for not significant.

More comprehensive details of fabrication processes, device structures, and performance characteristics appear in *SI Appendix*. Operation of the in vivo test of the SWB neural interface, theoretical analysis of SiN_x and MXene dissolution are also in *SI Appendix*.

Data, Materials, and Software Availability. Study data are included in the article and/or *SI Appendix*.

ACKNOWLEDGMENTS. This work is supported by the STI 2030-Major Project (2022ZD0209900), the National Key Technologies R&D Program of China (2021YFA0715302), the National Natural Science Foundation of China (62204057, 62304044), Lingang Laboratory (LGL-8998-09), Science and Technology Commission of Shanghai Municipality (22ZR1406400), State Key Laboratory of Integrated Chips and Systems (SKLICS-Z202306), National Key R&D Program of China (2022YFB3204800), and Strategic Priority Research Program of the Chinese Academy of Sciences (XDB0670000). We also appreciate the support by Shanghai Municipal Science and Technology Major Project (2018SHZDX01), ZJ Lab, Shanghai Center for Brain Science and Brain-Inspired Technology, the young scientist project of MOE innovation platform, and the China Postdoctoral Science Foundation (2023M730712). Part of the experiment work was carried out in Fudan Nanofabrication Laboratory.

Author affiliations: [a]Institute of Optoelectronics and College of Future Information Technology, College of Intelligent Robotics and Advanced Manufacturing, Shanghai Frontiers Science Research Base of Intelligent Optoelectronics and Perception, Fudan University, Shanghai 200438, China; [b]International Institute for Intelligent Nanorobots and Nanosystems & State Key Laboratory of Surface Physics, Fudan University, Shanghai 200438, China; [c]Zhejiang Key Laboratory of Extreme Environment Functional Materials, Yiwu Research Institute of Fudan University, Yiwu, Zhejiang 322000, China; [d]School of Mechanics and Aerospace Engineering, State Key Laboratory of Structural Analysis, Optimization and Computer Aided Engineering Software for Industrial Equipment, and International Research Center for Computational Mechanics, Dalian University of Technology, Dalian, Liaoning 116024, China; [e]Department of Ophthalmology, Tongji Hospital, School of Medicine, Tongji University, Shanghai 200065, China; [f]State Key Laboratory of Integrated Chips and Systems, Fudan University, Shanghai 200438, China; and [g]Neuromodulation and Brain-Machine-Interface Centre and Ministry of Education Frontiers Center for Brain Science, Fudan University, Shanghai 200438, China

Author contributions: P.L., L.Z., Y.L., G.H., Y.M., R.L., and E.S. designed research; P.L., L.Z., D.X., D.A., B.H., Y.S., and L.C. performed research; P.L., D.X., D.A., Y.L., N.H., C.G., L.C., Jinbao Li, Jiahao Li, F.L., J.L., G.H., Y.M., R.L., and E.S. contributed new reagents/analytic tools; P.L., B.H., Y.S., N.H., C.G., Jinbao Li, Jiahao Li, F.L., and E.S. analyzed data; and P.L., L.Z., D.X., R.L., and E.S. wrote the paper.

1. J. Koo *et al.*, Wireless bioresorbable electronic system enables sustained nonpharmacological neuroregenerative therapy. *Nat. Med.* **24**, 1830–1836 (2018).
2. H.-Y. Ahn *et al.*, Bioresorbable, wireless dual stimulator for peripheral nerve regeneration. *Nat. Commun.* **16**, 4752 (2025).
3. J. Scheib, A. Höke, Advances in peripheral nerve regeneration. *Nat. Rev. Neurol.* **9**, 668–676 (2013).
4. M. Mahar, V. Cavalli, Intrinsic mechanisms of neuronal axon regeneration. *Nat. Rev. Neurosci.* **19**, 323–337 (2018).
5. L. Dvali, S. Mackinnon, The role of microsurgery in nerve repair and nerve grafting. *Hand Clin.* **23**, 73–81 (2007).
6. A. Beris, I. Gkiatas, I. Gelalis, D. Papadopoulos, I. Kostas-Agnantis, Current concepts in peripheral nerve surgery. *Eur. J. Orthop. Surg. Traumatol.* **29**, 263–269 (2019).
7. P. B. Hardy, B. Y. Wang, K. M. Chan, C. A. Webber, J. B. Senger, The use of electrical stimulation to enhance recovery following peripheral nerve injury. *Muscle Nerve* **70**, 1151–1162 (2024).
8. S. M. Won, L. Cai, P. Gutruf, J. A. Rogers, Wireless and battery-free technologies for neuroengineering. *Nat. Biomed. Eng.* **7**, 405–423 (2023).
9. D. Ghezzi *et al.*, A polymer optoelectronic interface restores light sensitivity in blind rat retinas. *Nat. Photonics* **7**, 400–406 (2013).
10. M. Silverå Ejneby *et al.*, Chronic electrical stimulation of peripheral nerves via deep-red light transduced by an implanted organic photocapacitor. *Nat. Biomed. Eng.* **6**, 741–753 (2022).
11. X. Fu *et al.*, A silicon diode–based optoelectronic interface for bidirectional neural modulation. *Proc. Natl. Acad. Sci. U.S.A.* **121**, e2404164121 (2024).
12. J. Yi *et al.*, Water-responsive supercontractile polymer films for bioelectronic interfaces. *Nature* **624**, 295–302 (2023).
13. G. Lee *et al.*, A bioresorbable peripheral nerve stimulator for electronic pain block. *Sci. Adv.* **8**, eabp9169 (2022).
14. J. T. Reeder *et al.*, Soft, bioresorbable coolers for reversible conduction block of peripheral nerves. *Science* **377**, 109–115 (2022).
15. Y. Zhang *et al.*, Millimetre-scale bioresorbable optoelectronic systems for electrotherapy. *Nature* **640**, 77–86 (2025).
16. Y. Zhang *et al.*, Climbing-inspired twining electrodes using shape memory for peripheral nerve stimulation and recording. *Sci. Adv.* **5**, eaaw1066 (2019).
17. L. Wang *et al.*, A biodegradable and restorative peripheral neural interface for the interrogation of neuropathic injuries. *Nat. Commun.* **16**, 1716 (2025).
18. C. Dong *et al.*, Electrochemically actuated microelectrodes for minimally invasive peripheral nerve interfaces. *Nat. Mater.* **23**, 969–976 (2024).
19. J. Estelrich, M. A. Busquets, Iron oxide nanoparticles in photothermal therapy. *Molecules* **23**, 1567 (2018).
20. M. Overchuk, R. A. Weersink, B. C. Wilson, G. Zheng, Photodynamic and photothermal therapies: Synergy opportunities for nanomedicine. *ACS Nano* **17**, 7979–8003 (2023).
21. X. Yi, Q.-Y. Duan, F.-G. Wu, Low-temperature photothermal therapy: Strategies and applications. *Research* **2021**, 9816594 (2021).
22. S. Wan *et al.*, Scalable ultrastrong MXene films with superior osteogenesis. *Nature* **634**, 1103–1110 (2024).
23. G. Li *et al.*, Photothermal responsive cell-laden PNIPAM self-rolling hydrogel containing dopamine enhanced MWCNTs for peripheral nerve regeneration. *Compos. Part B Eng.* **254**, 110551 (2023).
24. C. Hu *et al.*, Fabrication of Au-polydopamine blackspheres-loaded PLLA-(silk fibroin) scaffold with photothermal conversion in NIR-II biowindows for deep nerve regeneration. *Chem. Eng. J.* **489**, 151171 (2024).
25. Y. Hong *et al.*, NIR-responsive multifunctional artificial skin for regenerative wound healing. *Adv. Funct. Mater.* **34**, 2405876 (2024).
26. L. Wang *et al.*, A fully biodegradable and self-electrified device for neuroregenerative medicine. *Sci. Adv.* **6**, eabc6686 (2020).
27. K. Deisseroth, Optogenetics. *Nat. Methods* **8**, 26–29 (2011).
28. Y. Hu *et al.*, Conductive nerve guidance conduits based on morpho butterfly wings for peripheral nerve repair. *ACS Nano* **16**, 1868–1879 (2022).
29. W. Huang *et al.*, Monolithic mtesla-level magnetic induction by self-rolled-up membrane technology. *Sci. Adv.* **6**, eaay4508 (2020).
30. W. Huang *et al.*, Three-dimensional radio-frequency transformers based on a self-rolled-up membrane platform. *Nat. Electron.* **1**, 305–313 (2018).
31. Z. Huang *et al.*, Two-dimensional MXene-based materials for photothermal therapy. *Nanophotonics* **9**, 2233–2249 (2020).
32. S. Zhang *et al.*, Engineered MXene biomaterials for regenerative medicine. *ACS Nano* **19**, 9590–9635 (2025).
33. E. Serger *et al.*, The gut metabolite indole-3 propionate promotes nerve regeneration and repair. *Nature* **607**, 585–592 (2022).
34. B. Merle, M. Göken, Fracture toughness of silicon nitride thin films of different thicknesses as measured by bulge tests. *Acta Mater.* **59**, 1772–1779 (2011).
35. R. Szabo, N. Sharkey, Response of peripheral nerve to cyclic compression in a laboratory rat model. *J. Orthop. Res.* **11**, 828–833 (1993).
36. T. Malik, A. Malik, A. Abd-Elsayed, Pathophysiology of work-related neuropathies. *Biomedicines* **11**, 1745 (2023).
37. Y. H. Jung *et al.*, A wireless haptic interface for programmable patterns of touch across large areas of the skin. *Nat. Electron.* **5**, 374–385 (2022).
38. K. Lim *et al.*, Interference haptic stimulation and consistent quantitative tactility in transparent electrotactile screen with pressure-sensitive transistors. *Nat. Commun.* **15**, 7147 (2024).
39. I. Oshina, J. Spigulis, Beer–lambert law for optical tissue diagnostics: Current state of the art and the main limitations. *J. Biomed. Opt.* **26**, 100901 (2021).
40. H. Jonasson *et al.*, In vivo characterization of light scattering properties of human skin in the 475-to 850-nm wavelength range in a Swedish cohort. *J. Biomed. Opt.* **23**, 121608 (2018).
41. D. Nelidova *et al.*, Restoring light sensitivity using tunable near-infrared sensors. *Science* **368**, 1108–1113 (2020).
42. X. Wu *et al.*, Tether-free photothermal deep-brain stimulation in freely behaving mice via wide-field illumination in the near-infrared-II window. *Nat. Biomed. Eng.* **6**, 754–770 (2022).
43. Y. Lyu, C. Xie, S. A. Chechetka, E. Miyako, K. Pu, Semiconducting polymer nanobioconjugates for targeted photothermal activation of neurons. *J. Am. Chem. Soc.* **138**, 9049–9052 (2016).
44. Y. Fu, W. J. Kao, Drug release kinetics and transport mechanisms of non-degradable and degradable polymeric delivery systems. *Expert Opin. Drug Deliv.* **7**, 429–444 (2010).
45. N. Kamaly, B. Yameen, J. Wu, O. C. Farokhzad, Degradable controlled-release polymers and polymeric nanoparticles: Mechanisms of controlling drug release. *Chem. Rev.* **116**, 2602–2663 (2016).
46. C. Corsaro, G. Neri, A. M. Mezzasalma, E. Fazio, Weibull modeling of controlled drug release from Ag–PMA nanosystems. *Polymers* **13**, 2897 (2021).
47. M. Barzegar-Jalali, Kinetic analysis of drug release from nanoparticles. *J. Pharm. Pharm. Sci.* **11**, 167–177 (2008).
48. A. Bozkurt *et al.*, Catwalk gait analysis in assessment of functional recovery after sciatic nerve injury. *J. Neurosci. Methods* **173**, 91–98 (2008).
49. E. Song *et al.*, Transferred, ultrathin oxide bilayers as biofluid barriers for flexible electronic implants. *Adv. Funct. Mater.* **28**, 1702284 (2018).
50. H. Fang *et al.*, Ultrathin, transferred layers of thermally grown silicon dioxide as biofluid barriers for biointegrated flexible electronic systems. *Proc. Natl. Acad. Sci. U.S.A.* **113**, 11682–11687 (2016).
51. P. Froeter *et al.*, Toward intelligent synthetic neural circuits: Directing and accelerating neuron cell growth by self-rolled-up silicon nitride microtube array. *ACS Nano* **8**, 11108–11117 (2014).
52. S.-K. Kang *et al.*, Dissolution behaviors and applications of silicon oxides and nitrides in transient electronics. *Adv. Funct. Mater.* **24**, 4427–4434 (2014).
53. T. R. Dmytriv, V. I. Lushchak, Potential biosafety of Mxenes: Stability, biodegradability, Toxicity and biocompatibility. *Chem. Record* **24**, e202300338 (2024).
54. C. J. Zhang *et al.*, Oxidation stability of colloidal two-dimensional titanium carbides (MXenes). *Chem. Mater.* **29**, 4848–4856 (2017).
55. X. Zhao *et al.*, pH, Nanosheet concentration, and antioxidant affect the oxidation of $Ti_3C_2T_x$ and Ti_2CT_x MXene dispersions. *Adv. Mater. Interfaces* **7**, 2000845 (2020).
56. H. Lin, S. Gao, C. Dai, Y. Chen, J. Shi, A two-dimensional biodegradable niobium carbide (MXene) for photothermal tumor eradication in NIR-I and NIR-II biowindows. *J. Am. Chem. Soc.* **139**, 16235–16247 (2017).
57. S. Gou *et al.*, Applications of 2D nanomaterials in neural interface. *Int. J. Mol. Sci.* **25**, 8615 (2024).
58. Y. Wang *et al.*, $Ti_3C_2T_x$ MXene flakes for optical control of neuronal electrical activity. *ACS Nano* **15**, 14662–14671 (2021).
59. S. Shankar *et al.*, Transparent MXene microelectrode arrays for multimodal mapping of neural dynamics. *Adv. Healthc. Mater.* **14**, 2402576 (2025).
60. E. Obeng *et al.*, MXene-chitosan photo-responsive conduit for wireless optogenetic stimulation to enhance neural regeneration and functional recovery after optic nerve injury. *Acta Biomater.* **205**, 205–221 (2025).